Technical Communication

Pulse Duration and Wavelength Effects on the Surface Topography of Direct Laser Interference Patterning Treated Titanium Specimen

Frederic Schell*[1], Avinash Hariharan[2], Phil Goldberg[2], Robert Baumann[3], Erwin Jäger[4], Annett Gebert[2], Christoph Zwahr[1], and Andrés F. Lasagni[1,3]

[1]*Fraunhofer Institute for Material and Beam Technology IWS, Winterbergstr. 28, 01277 Dresden, Germany*
[2]*Leibniz Institute for Solid State and Materials Research Dresden, Helmholtzstr. 20, 01069 Dresden, Germany*
[3]*Institut für Fertigungstechnik, Technische Universität Dresden, George-Bähr-Str. 3c, 01069 Dresden, Germany*
[4]*TOPAG Lasertechnik GmbH, Nieder-Ramstädter Str. 247, 64285 Darmstadt, Germany*
*Corresponding author's e-mail: frederic.schell@iws.fraunhofer.de

With rising prevalence of bone and skeletal diseases around the world, combatting implant failure through novel approaches has become a growing area of research. A novel way to produce tailored implants is additive manufacturing, which offers unprecedented design flexibility. On the other hand, the osseointegration of such implants can be optimized by applying periodic micro-textures on the surface, using laser-based techniques. In particular, the technique of Direct Laser Interference Patterning (DLIP) offers both high throughput and the possibility to produce structures with small feature sizes. In this work, DLIP is applied to produce line-like micro textures on additively manufactured Ti-13Nb-13Zr parts. Using different solid-state lasers, the effect of pulse durations in the nanosecond to femtosecond regime and laser wavelengths from the ultraviolet to near infrared spectrum on the micro texture topography is reported. For each wavelength and pulse duration, laser parameters are varied systematically. The surface topography of the specimens is characterized through scanning-electron microscopy, and surface roughness is measured with confocal microscopy. Interaction with nanosecond pulses is characterized by melting, resulting in mostly smooth textures, whereas picosecond and femtosecond pulses produce hierarchical textures with laser-induced periodic surface structures.
DOI: 10.2961/jlmn.2022.03.3002
Keywords: microtextures, direct laser interference patterning, nanosecond, picosecond, femtosecond, additive manufacturing

1. Introduction

For biomedical applications, the usage of biocompatible materials is of utmost importance. As such, titanium alloys are widespread for the fabrication of implants due to their non-toxicity and advantageous properties for osseointegration. Implants often require geometries individually tailored to the specific application and patient. Therefore, manufacturing processes that can rapidly fabricate individual and flexible geometries are necessary. One such technology that fulfills these requirements is laser powder-bed fusion (LPBF), where the layer-wise building of the material allows for fabrication of complex geometries that cannot be manufactured using classical machining techniques. The potential of additive manufacturing for increasing osseointegration, for instance through increasing the bone to implant contact area, has already been reported [1,2].

Although titanium already constitutes a material with advantageous properties for osseointegration, an improvement of those properties through non-biohazardous surface modifications is desirable. It was already demonstrated that microscopic surface modifications can be employed to enhance anti-bacterial effects [3–6] and promote cell adhesion [7–9]. Surface microtextures can be achieved through various surface microtexturing techniques, like micromachining and lithography, among which laser-based approaches have the advantage of requiring only a single processing step for the fabrication of microstructures and allowing for great flexibility regarding structure design.

A well-established laser-based technique for the creation of micro- to nanoscale surface features relies on the generation of laser-induced periodic surface structures (LIPSS) that can predominantly be observed on materials irradiated with short and ultrashort pulsed lasers. A wide variety of LIPSS are classified in the literature, however, the main distinction is drawn between low spatial frequency LIPSS (LSFL), which exhibit periodicities close to the laser wavelength ($\Lambda \sim \lambda$), and high spatial frequency LIPSS (HSFL) with $\Lambda < \lambda/2$. On metals, LSFL mainly occur perpendicular to the beam polarization vector [10].

Direct Laser Interference Patterning (DLIP) has also been established as a viable alternative to conventional techniques, such as Direct Laser Writing (DLW). It offers higher processing speeds [11] and the ability to produce microstructures inside a single laser pulse [12]. DLIP has been successfully used to produce complex micropatterns on a

wide variety of materials, such as polymers [13], ceramics [14], thin films [15] and different metals [16–18]. In recent years, it was shown that DLIP microtextures can enhance osseointegration in metallic parts [19,20].

When using pulsed laser sources, the laser-material interaction is strongly dependent on the pulse duration. The interaction mechanism of nanosecond pulses is predominantly characterized by melting and evaporation as well as melt expulsion due to recoil pressure [21,22]. On the other hand, the extreme energy densities of ultrashort pulses in the femto- to picosecond regime enable significant non-linear absorption effects as well as phase explosions, where overheated liquid expands rapidly [23]. The heat affected zone is also reduced as a consequence of significantly shorter thermal diffusion lengths [23].

The research presented here builds on previously reported results concerning the optimization of LBPF process parameters for fabrication of Ti-13Nb-13Zr alloy [24] as well as microtexturing of the alloy using Direct Laser Interference Patterning [25,26].

This work aims to produce a feasibility study regarding the microtexturing of additively manufactured Ti-13Nb-13Zr specimens by using DLIP. To this end, the effects of pulse duration and wavelengths on the morphology are investigated using different laser sources that emit pulses in the nanosecond, picosecond and femtosecond regime as well as near-infrared, visible and ultraviolet radiation.

2. Materials and Methods

As a substrate material, 1 mm thick near-beta Ti-13Nb-13Zr alloy samples were fabricated using the LPBF process. Prior to the laser structuring, the samples were grinded with a grain size of 1200, reaching an initial surface roughness value of S_a = 0.21 ± 0.05 µm. Moreover, all samples were cleaned with ethanol prior to the laser treatment.

The structuring experiments were performed using different DLIP setups in a two-beam configuration. The experimental setups all consist of a laser source, an optical assembly responsible for splitting the beams and overlapping them at a specific angle on the substrate, and a three-axis positioning system consisting of three linear high precision stages (Aerotech). Two horizontal stages are used to translate the substrate relative to the laser beam, while the optical assembly is mounted on a third vertical stage used to adjust the working position. The experiments are performed using the laser sources listed in **Table 1**, which cover pulse durations from femtoseconds to nanoseconds and wavelengths from ultraviolet (UV) over visible (VIS) to infrared (IR) light and provide a near Gaussian beam distribution.

The DLIP optical assembly (**Figure 1a**) consists of a diffractive optical element (DOE) that splits the laser beam into two sub-beams that are subsequently parallelized by a prism and overlapped on the substrate by a converging lens. The spatial period of the emerging interference pattern can thereby be easily controlled by adjusting the position of the prism relative to the DOE. The experiments with the femtosecond laser source employed a slightly different optical configuration, where the sub-beams split by the DOE are parallelized by a half-cylinder converging lens at a distance to the DOE of exactly its focal length. Another half cylinder lens oriented perpendicular to the first lens is used to focus the beam in one axis. Lastly, the beams are overlapped on the substrate by a third half-cylinder lens at a distance from the first lens equal to the sum of both their focal lengths. This produces a laser spot elongated perpendicular to the structuring direction and focused along the structuring direction, with the dimensions 160 µm x 1000 µm.

Table 1 Properties of laser sources employed for the experiments

Laser source	τ (s)	λ (nm)	M^2	$E_{p,max}$ (µJ)
TECH-527 Advanced, Laser-Export	$5 \cdot 10^{-9}$	527	< 1.2	500
TECH-1053 Basic, Laser-Export	$6 \cdot 10^{-9}$	1053	< 1.2	500
Innoslab Nd:YV04, Edgewave	$10 \cdot 10^{-12}$	355, 532, 1064	< 1.1	500
Carbide CB3-40W, Light Conversion	$266 \cdot 10^{-15}$	1030	< 1.2	400

In order to fabricate long range homogeneous structures, the samples were translated by means of motorized linear stages in the x- and y-direction. Thereby, individual pulses were arranged over the surface and overlapped by the pulse-to-pulse overlap in the primary moving direction (parallel to the interference lines), generating lines of structured materials (**Figure 1b**). Those lines were overlapped in the secondary moving direction by the hatch distance h, which was set to an integer multiple of the spatial period. The overlap is tangibly expressed as the number of pulses per pixel *N*, where *d* is the interference diameter and *p* is the pulse-to-pulse distance (see Eq. 5).

$$N = \frac{d}{p} \tag{5}$$

Alternatively, the pulse-overlap in the vertical axis (as a percentage value of the beam diameter) can be calculated as shown in Eq. 6.

$$O = 1 - \frac{1}{N} = 1 - \frac{p}{d}\,[\%] \tag{6}$$

The fluence values for every laser source were retrieved by measuring the laser power in the interference area with a power meter and estimating the characteristic Gaussian beam diameter at $1/e^2$ in the interference area according to the D-squared method proposed by Liu [27], yielding the average fluence as the quotient of pulse energy and irradiated area. For nanosecond and picosecond laser sources, the ablation thresholds were also estimated using this method.

2.1 Characterization

The sample surfaces were characterized by means of laser-scanning confocal microscopy (LSM) employing a violet laser at a wavelength of 408 nm (VK-X200K, Keyence). The LSM measurements were conducted with 50 X and 150 X magnification objectives with a measurement area of 270 x 90 µm² and 90 x 67 µm² respectively. The resolution amounts to 0.5 nm for height measurements and 1 nm for width measurements. All measurements are performed with

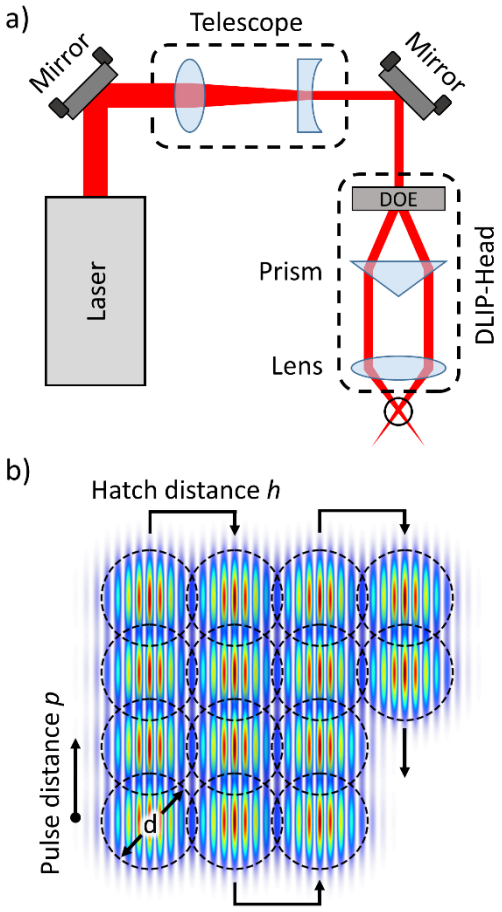

Fig. 1 Schematic of a) the experimental setup and b) the structuring strategy. The sample is translated vertically between pulses by the pulse distance and translated between lines of pulses by the hatch distance, which equals an integer multiple of the spatial period.

the highest available measurement quality providing 2048 x 1536 pixels per frame and repeated four times on different areas of each structured surface in order to obtain the mean and standard deviation of the parameters. Measurement files were evaluated using the software LeicaMap to calculate the surface parameters according to ISO 25178.

The morphology of the samples was furthermore characterized using a scanning electron microscope (SEM) at 15 kV of operating voltage (JSM 6610LV, JEOL). The LIPSS period is measured using high resolution SEM images and using the software ImageJ, averaging over a minimum of 10 periods.

Spectroscopy measurements are performed on a spectrometer ranging from UV to near-IR (Varian Cary 5000 UV-Vis-NIR) and an integrating sphere with spectralon.

3. Results and discussion

In a first step, wavelength dependent reflectivity of grinded Ti-13Nb-13Zr is measured using a spectrometer. **Figure 2** shows that the reflectivity increases with increasing wavelength, almost doubling from approximately 20 %, using a wavelength 355 nm, to 38%, using a wavelength of 532 nm. Up to the near infrared regime with 1064 nm, a moderate increase to 53 % reflectivity is observed. Therefore, shorter wavelengths provide better efficiency by utilizing more of the incident radiation for material treatment. However, the conversion from the fundamental (1064 nm) to the second (532 nm) and third (355 nm) harmonic are accompanied by significant conversion losses [28,29].

In a second step, line-like textures are fabricated with laser sources in the nanosecond, picosecond and femtosecond pulse duration regime on pre-grinded Ti-13Nb-13Zr specimens.

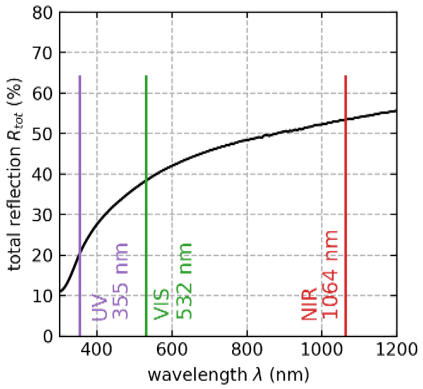

Fig. 2 Total reflection of grinded Ti-13Nb-13Zr measured using a spectrometer with the laser wavelengths marked by vertical lines. The reflectivity decreases significantly for shorter wavelengths.

3.1 Nanosecond-pulsed texturing

Using nanosecond pulses, specimens were textured with a wavelength of 532 nm and 1053 nm. The period was fixed at a value of 5 µm and the hatch distance was fixed at a value of 40 µm and 15 µm for a wavelength of 527 nm and 1053 nm, respectively. The number of pulses and the fluence per pulse were varied systematically. For each laser wavelength, selected textures fabricated at three different cumulated fluences are shown in **Figure 3**. It can be observed that both wavelengths yield regular periodic line-like microtextures. However, the morphology differs insofar as the textures fabricated with 532 nm (**Figure 3a-c**) feature recurring spherical protrusions along the fringes. Their prevalence and size increased with increasing cumulated fluence. Due to the fact that for ns-pulses the structuring mechanism is based in the Marangoni convection, molten material at the interference maxima positions flows to the minima positions due to the induced thermal gradient [30,31]. On the other hand, textures fabricated with 1053 nm and a period of 5 µm (**Figure 3d-e**) show more regular lines. However, as it can be seen in **Figure 3e**, the valleys of the topography show discontinuous depths with randomly distributed hole-like dents. These could originate from slight inhomogeneities in the material surface caused by the LBPF manufacturing process. Using a fluence of 1.82 J/cm² and 11 pulses, localized joining of the structure peaks can be observed, as shown in **Figure 3f**.

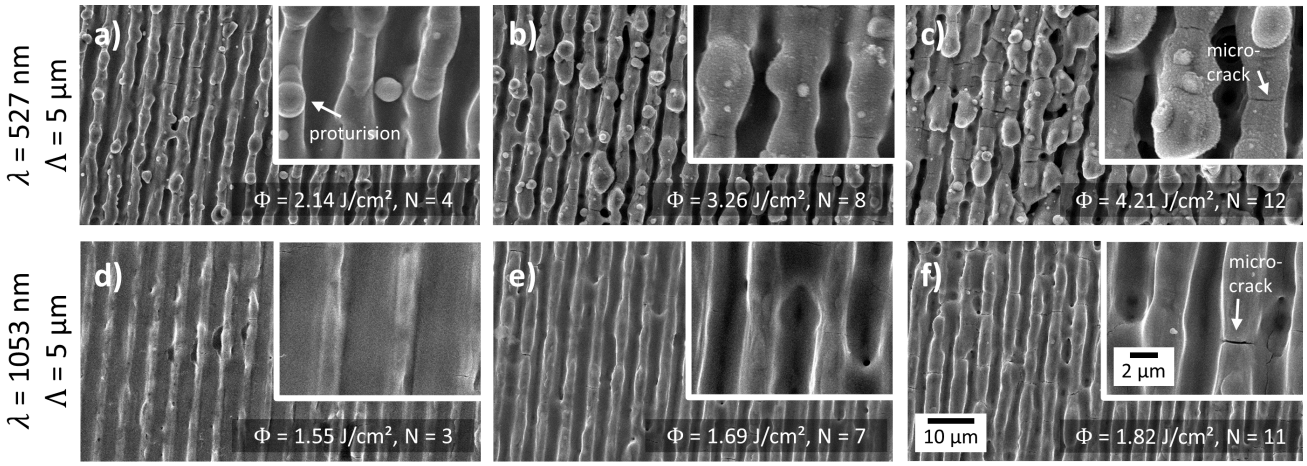

Fig. 3 SEM images of selected nanosecond-pulse textured specimens, using a spatial period of 5 µm and a wavelength of a) – c) 532 nm and d – f) 1053 nm. The cumulated fluence is increased from left to right (increased number of pulses and fluence).

Furthermore, the formation of micro-cracks can be observed on all nanosecond-textured surfaces, which increase in size and prevalence. These cracks are a result of high heat accumulation during nanosecond texturing. Since the timescale of the pulses is long compared to the electron-lattice relaxation time, a large amount of energy from the incident radiation can be transferred to the lattice structure, resulting in crack formation. Moreover, the used laser fluences are significantly higher than the determined ablation threshold of 0.83 J/cm² at 1053 nm.

After the laser processing, the fabricated textures were characterized using a confocal microscope and evaluated in terms of their arithmetic mean height, as shown in **Figure 4**. The pulse fluence and number of pulses per spot are varied over 5 defined intervals, yielding a total of 25 different surface textures. Generally, increasing the fluence and number of pulses results in higher roughness values. However, the fluence does not exert as strong an effect on the roughness for textures fabricated with 527 nm, as observed in **Figure 4a**. This could be related to the generally high pulse fluences chosen, compared to textures fabricated with 1053 nm. Moreover, the maximum value of Sa of 1.50 ± 0.05 µm is achieved using a fluence of 3.26 J/cm². When the maximal fluence of 4.21 J/cm² is used, the value decreases again by 0.1 µm, which can be explained by the frequently occurring filling of the structure valleys with molten material, which is observed in **Figure 3c**. The local minimum at 10 pulses and 3.26 J/cm² close to the global maximum is likely a result of both local texture inhomogeneity and random selection of measurement area. This assumption is supported by the relatively high error bar compared to the surrounding values.

Using a wavelength of 1053 nm, a maximum arithmetic mean height of 1.00 ± 0.03 µm is achieved for the highest employed number of pulses (11) and the highest fluence (1.82 J/cm²), as shown in **Figure 4b**. A local maximum is not observed, and the gradient of the roughness as a function of the pulse number and fluence indicates that a further increase of the parameters might result in higher roughness values.

3.2 Picosecond-pulsed texturing

Using a picosecond-pulse laser source equipped with a second and third harmonic generator, line-like DLIP textures are fabricated with a fixed spatial period of 5µm and wavelengths of 355 nm, 532 nm and 1064 nm. Selected SEM images are given in **Figure 5**. The cumulated fluence increased from left to right by increasing either the single pulse fluence or number of pulses. Similar to the nanosecond textures, the

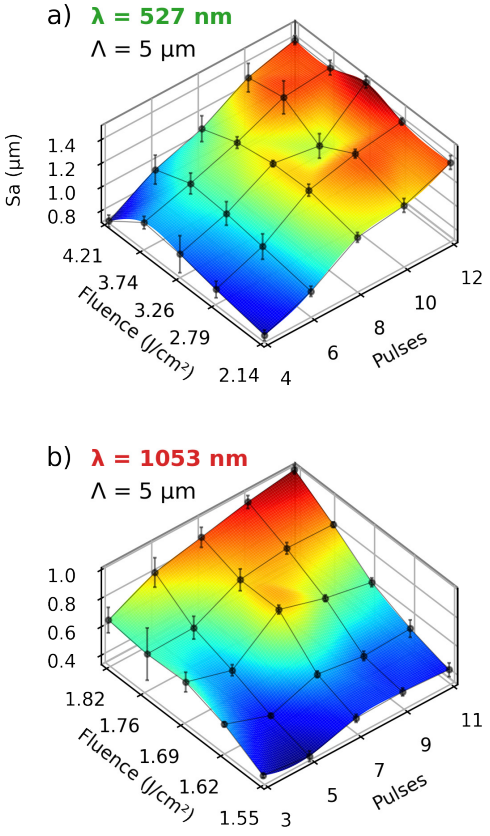

Fig. 4 Maps of arithmetic mean height (Sa) for varying fluence and pulse overlap using nanosecond-pulsed lasers with Λ = 5 µm and a) λ = 532 nm, h = 8Λ, b) λ = 1053 nm, h = 3Λ.

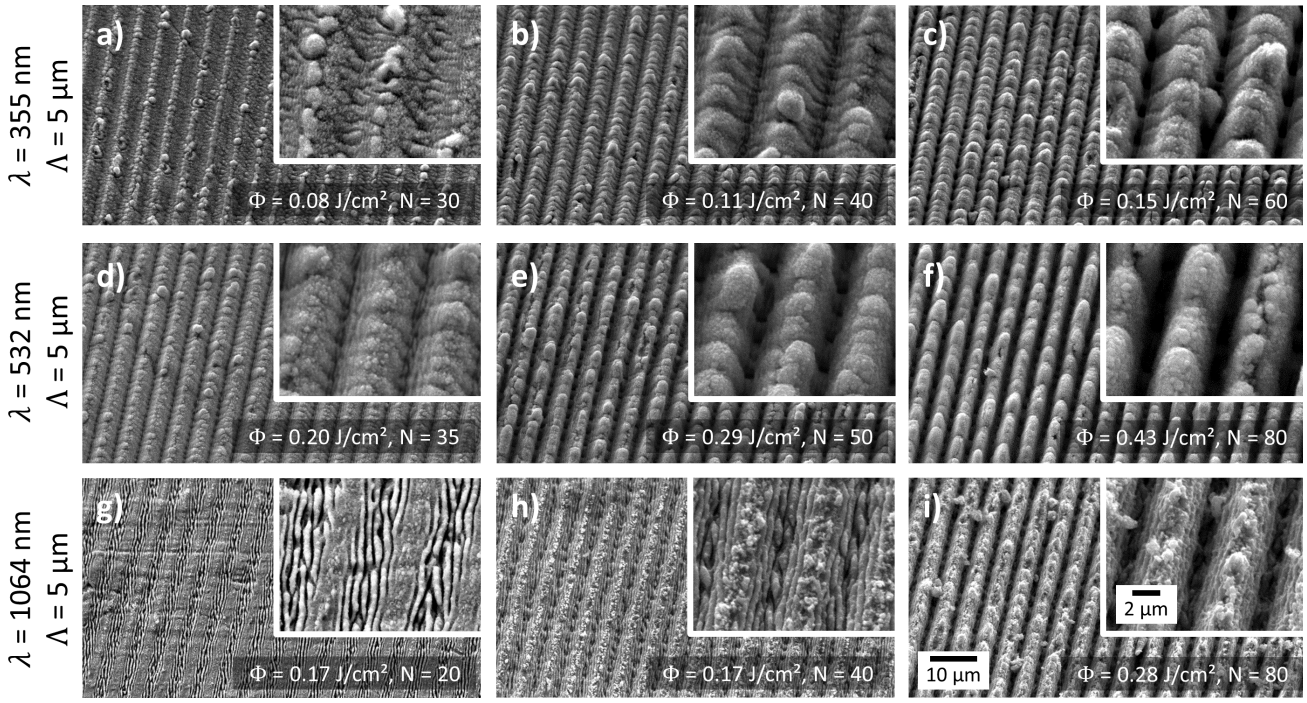

Fig. 5 SEM images of selected picosecond-pulse textured specimens, using a wavelength of a) – c) 355 nm, d – f) 532 nm and h) – h) 1064 nm as well as a spatial period of 5 µm. The cumulated fluence is increased from left to right (increased number of pulses and fluence).

structure depth increases with increasing cumulated fluence. However, compared to nanosecond textures fabricated with a period of 5 µm, melting is substantially reduced.

Moreover, picosecond-pulsed irradiation produces hierarchical surface features in the form LIPSS, as previously reported on [25,26]. The period of the LSFL and HSFL hereby depends on the laser wavelength. Shorter wavelengths are directly correlated to smaller LSFL and HSFL periods. The averaged LIPSS period as a fraction of the laser wavelength used for fabrication of the textures is listed in **Table 2**. Generally, LSFL are produced at around 0.7 times, and the HSFL at around 0.2 times the laser wavelength. The LSFL are thereby oriented in parallel to the DLIP textures and perpendicular to the polarization of the laser, while the HSFL are oriented in parallel to the DLIP textures and alongside the laser polarization. Using low cumulated fluences, the regions of the interference maxima are predominantly covered with LIPSS (see **Figure 5d**), whereas using high cumulated fluences results in DLIP textures becoming the dominant topographical feature.

Furthermore, supra-wavelength grooves occur parallel to the electric field vector on textures fabricated with 355 nm and 532 nm, however not on textures fabricated with 1064 nm. This can be explained by the threshold fluence for groove formation decreasing with decreasing wavelengths [32]. On the other hand, the groove period increases linearly with the cumulated fluence as previously reported [25].

The formation of microcracks is observed less frequently than when using nanosecond pulsed lasers. In this case, the heat dissipation is reduced due to the short pulses, in turn reducing the potential for crack formation. Nonetheless, using a fluence of 0.43 J/cm², a pulse number of 80 and a wavelength of 532 nm (see **Figure 5f**), a large crack along

Table 2 LIPSS period as a fraction of the utilized laser wavelength averaged over all measured textures per wavelength.

LIPSS-Period	λ = 355 nm	λ = 532 nm	λ = 1064 nm
LSFL	0.69 ±0.05	0.76 ± 0.12	0.58 ±0.09
HSFL	0.25 ±0.01	0.20 ±0.02	0.16 ±0.02

the DLIP structure peak is observed. However, this could be rather related to the incomplete joining of recast material from the regions of the interference minima, as reported by Lang et al. [33]. The difference compared to nanosecond pulses could be related to the significantly lower fluences employed compared to the single pulse ablation thresholds (355 nm: 0.35 J/cm², 532 nm: 0.41 J/cm², 1064 nm: 0.65 J/cm² [26]). While the used single pulse fluences were close to and below the respective threshold values, the high overlap compared to nanosecond pulse experiments can be assumed to reduce the multi-pulse threshold significantly according to the incubation effect [34]).

The arithmetic mean height of the analyzed textures was found to gradually increase with an increasing number of pulses and pulse fluence. Using a wavelength of 355 nm, a maximum value of Sa of 1.19 ± 0.01 µm is reached for 60 pulses and 0.11 J/cm², as shown in **Figure 6a**. A further increase of the fluence up to 0.15 J/cm² results in a slight decrease of Sa to 1.15 µm again. For 532 nm, the larger chosen parameter window shows that a maximum of 1.35 ± 0.08 µm is already reached for 50 pulses and 0.29 J/cm², as shown in **Figure 6b**. Increasing the pulse

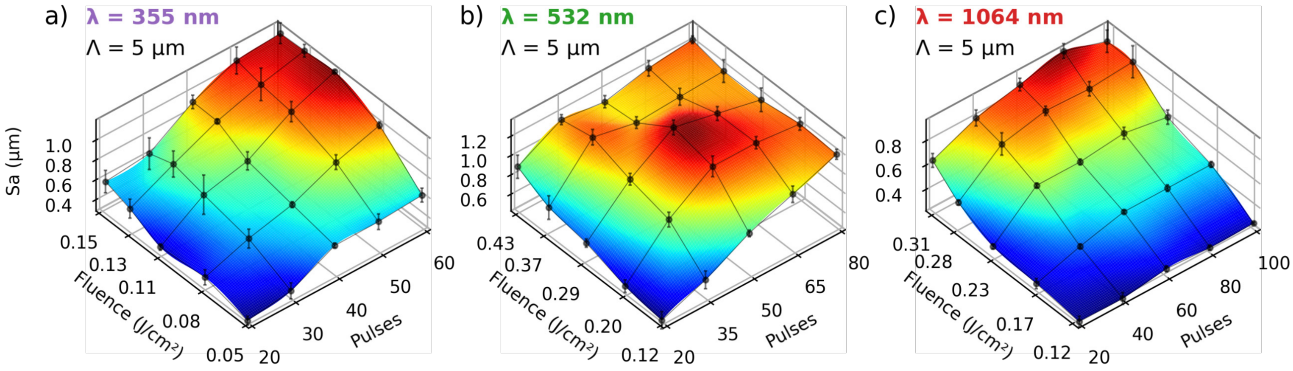

Fig. 6 Maps of arithmetic mean height (Sa) for varying fluence and pulse overlap using picosecond-pulsed lasers with Λ = 5 µm a) λ = 355 nm, h = 3Λ, b) λ = 532 nm, h = 2Λ, c) λ = 1064 nm, h = 2Λ.

number and fluence beyond these values results in a decrease of Sa, which transitions to a plateau at an approximate value of 1.18 ± 0.03 µm.

Utilizing a wavelength of 1064 nm, the number of pulses only exerts a significant effect on Sa between 20 and 60 pulses, as visualized in F**igure 6c**. Using higher pulse numbers up to 100, Sa remains steady for fixed fluence values. The fluence, on the other hand, strongly correlates with higher Sa values, reaching a maximum value of 0.96 ± 0.06 µm for 80 pulses and 0.31 J/cm². Here, the stagnating roughness as a function of the number of pulses can be explained by the large parameter window chosen and by saturation effects dominating after a pulse number of 60.

3.3 Femtosecond-pulsed texturing

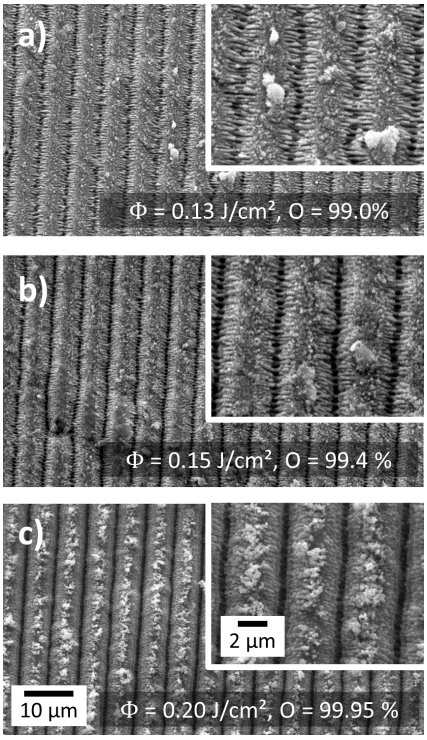

Fig. 7 SEM images of selected femtosecond-pulse textured specimens, using a wavelength of 1030 nm and spatial period of 6 µm. The cumulated fluence is increased from top to bottom (increased number of pulses and fluence).

Finally, textures were fabricated using a laser source with 266 fs pulse width, a wavelength of 1030 nm and a spatial period of 6 µm.

The morphology of three selected textures with increasing cumulated fluence is shown in **Figure 7**. The employed fluences were close to and slightly above the single pulse ablation threshold (~0.1 J/cm² as determined with 500 fs and 1030 nm on Ti-6Al-4V [35]). However, it can be assumed that the very high pulse overlap used in the experiments decreased the threshold fluence for multi-pulse processing significantly according to the incubation effect [34]. Similar to the nanosecond and picosecond processed samples, the texture depth increases with increasing cumulated fluence. LSFL are observed perpendicular to the DLIP textures and to the polarization vector, ranging from the top of the structure peaks towards the structure valleys. Their period was estimated to 444 ± 39 nm using SEM images. As a fraction of the laser wavelength, the LSFL period is approximately 0.43. This value is atypically small compared to values found on ps-treated textures as well those reported in the literature, which generally lie around 0.9 λ [36]. However, LSFL with $\Lambda_{LSFL} < 0.5\lambda$ have been observed on DLIP-treated metals before by Alamri et al. [37] and Sikora et al. [38] and were attributed to the interplay between LIPSS formation and DLIP processing. Moreover, multiple effects could be involved in explaining the observed period. In a

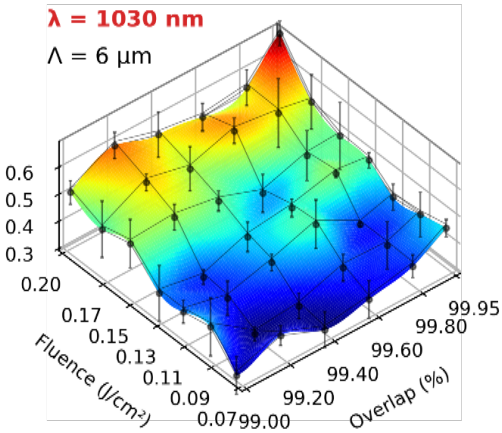

Fig. 8 Map of arithmetic mean height (Sa) for varying fluence and pulse overlap using a femtosecond-pulsed laser with a) λ = 1030 nm and Λ = 6 µm.

specific fluence regime, LSFL have been observed to split, which results in half the expected periodicity [39,40]. Furthermore, the LIPSS period is known to decrease with an increasing number of pulses [41], which could play an important role in our case since N lies between 100 and 2,000. Lastly, the high photon densities of femtosecond pulses could result in non-linear phenomena, such as second harmonic (SH) generation. In that case, the LSFL period would correspond to $0.83 \pm 0.07\ \lambda_{SH}$, which is close to the expected fraction.

Figure 8 shows the roughness map of textures fabricated with a spatial period of 6 µm and varying fluence and pulse overlap. Here, pulse-overlap is given according to equation 6, since near constant intervals are chosen on the basis of that representation and would result in strongly uneven spacing in the representation given in equation 5. Similar to the other pulse durations, higher fluences result in increased arithmetic mean height. On the other hand, the pulse overlap in the chosen parameter window does not exert a significant influence on the arithmetic mean height. Since the number of pulses per spot is comparatively high (99.0 % and 99.95 % pulse overlap are equivalent to 100 and 2000 pulses, respectively), a saturation behavior can be presumed. This can explain the relatively negligible influence of the pulse overlap on the surface roughness.

8. Conclusions

In this work, laser surface texturing by means of Direct Laser Interference Patterning was applied to a novel near-beta Ti-13Nb-13Zr alloy. Microstructures fabricated with laser systems using different pulse durations ranging from femtoseconds to nanoseconds and wavelengths ranging from 355 nm to 1064 nm were investigated. Nanosecond laser pulses were shown to produce smooth single-scale textures but were prone to reducing visually assessed texture homogeneity due to melting effects caused by Marangoni convection.

Picosecond and femtosecond pulses resulted in the formation of LIPSS that function as a hierarchical structure on top of the interference-based geometry. The used laser wavelength showed to have influence on the morphology by determining the size of the LIPSS using the picosecond laser. Furthermore, the wavelength dependent absorption behavior of the Ti-13Nb-13Zr alloy had the effect that less fluence was required with shorter wavelengths to achieve similar surface roughness.

Lastly, using ultrashort pulses, the influence of melting could be reduced (picosecond pulses) and completely avoided (femtosecond pulses), making the texturing with small periods more viable.

In summary, this work is intended to serve as an exploratory basis for surface functionalization of Ti-13Nb-13Zr. It can be concluded that all tested wavelengths and pulse durations are generally suited to texture the investigated alloy with DLIP. Since the most defining characteristic of the textures as a result of pulse duration and wavelength was the occurrence and morphology of the LIPSS, new ongoing experiments will focus on investigating the effect of the presence of LIPSS on top of DLIP textures on biocompatibility.

Acknowledgments

This work was carried out in the framework of the project OsteoLas and partially financed by the European Regional Development Fund (EFRE) and by tax revenues on the basis of the budget adopted by the Members of the Parliament of Saxony (funding reference 100382988 / 100382989). We thank Dr. Tim Kunze for his work in drafting the project and Dr. Sabri Alamri for his help in acquiring some of the SEM images. Moreover, we thank Nadine Böhme for preparation of the sample surfaces and Willi Schell for proofreading.

References

[1] C. N. Kelly, T. Wang, J. Crowley, D. Wills, M. H. Pelletier, E. R. Westrick, S. B. Adams, K. Gall, and W. R. Walsh: Biomaterials, 279, (2021), 121206.
[2] B.-S. Lee, H.-J. Lee, K.-S. Lee, H. G. Kim, G.-H. Kim, and C.-W. Lee: Appl. Surf. Sci., 508, (2020), 145160.
[3] X. Luo et al.: Opt. Laser Technol., 124, (2020), 105973.
[4] A. H. A. Lutey, L. Gemini, L. Romoli, G. Lazzini, F. Fuso, M. Faucon, and R. Kling: Sci. Rep., 8, (2018), 10112.
[5] R. Helbig, D. Günther, J. Friedrichs, F. Rößler, A. Lasagni, and C. Werner: Biomater. Sci., 4, (2016), 1074.
[6] X. Zhang, L. Wang, and E. Levänen: RSC Adv., 3, (2013), 12003.
[7] L. Salou, A. Hoornaert, G. Louarn, and P. Layrolle: Acta Biomater., 11, (2015), 494.
[8] S. Dundar, F. Yaman, A. Bozoglan, T. T. Yildirim, M. Kirtay, M. F. Ozupek, and G. Artas: J. Craniofac. Surg., 29, (2018), 1991.
[9] A. T. Nguyen, S. R. Sathe, and E. K. F. Yim: J. Phys. Condens. Matter, 28, (2016), 183001.
[10] J. Bonse and S. Gräf: Laser Photonics Rev., 14, (2020), 2000215.
[11] M. Bieda, E. Beyer, and A. F. Lasagni: J. Eng. Mater. Technol., 132, (2010), 031015.
[12] S. Alamri, A. I. Aguilar-Morales, and A. F. Lasagni: Eur. Polym. J., 99, (2018), 27.
[13] D. Sola, C. Lavieja, A. Orera, and M. J. Clemente: Opt. Lasers Eng., 106, (2018), 139.
[14] D. Fabris, A. F. Lasagni, M. C. Fredel, and B. Henriques: Ceramics, 2, (2019), 578.
[15] B. Voisiat: J. Laser MicroNanoengineering, 6, (2011), 185.
[16] S. Alamri, V. Vercillo, A. I. Aguilar-Morales, F. Schell, M. Wetterwald, A. F. Lasagni, E. Bonaccurso, and T. Kunze: Adv. Mater. Interfaces, (2020), 2001231.
[17] J. T. Cardoso, A. I. Aguilar-Morales, S. Alamri, D. Huerta-Murillo, F. Cordovilla, A. F. Lasagni, and J. L. Ocaña: Opt. Lasers Eng., 111, (2018), 193.
[18] A. I. Aguilar-Morales, S. Alamri, and A. F. Lasagni: J. Mater. Process. Technol., 252, (2018), 313.
[19] C. Zwahr, R. Helbig, C. Werner, and A. F. Lasagni: Sci. Rep., 9, (2019), 6721.
[20] C. Zwahr, D. Günther, T. Brinkmann, N. Gulow, S. Oswald, M. Grosse Holthaus, and A. F. Lasagni: Adv. Healthc. Mater., 6, (2017), 1600858.

[21] B. Lauer, B. Jäggi, and B. Neuenschwander: Phys. Procedia, 56, (2014), 963.
[22] C. Momma, B. N. Chichkov, S. Nolte, F. von Alvensleben, A. Tünnermann, H. Welling, and B. Wellegehausen: Opt. Commun., 129, (1996), 134.
[23] K.-H. Leitz, B. Redlingshöfer, Y. Reg, A. Otto, and M. Schmidt: Phys. Procedia, 12, (2011), 230.
[24] A. Hariharan, P. Goldberg, T. Gustmann, E. Maawad, S. Pilz, F. Schell, T. Kunze, C. Zwahr, and A. Gebert: Mater. Des., (2022), 110618.
[25] F. Schell, S. Alamri, A. Hariharan, A. Gebert, A. F. Lasagni, and T. Kunze: Mater. Lett., 306, (2022), 130920.
[26] F. Schell, A. Hariharan, P. Goldberg, S. Alamri, A. Gebert, T. Kunze, and A. F. Lasagni: Proc. Laser-based Micro- and Nanoprocessing XVI, (2022), 43.
[27] J. M. Liu: Opt. Lett., 7, (1982), 196.
[28] H. Zhu, T. Wang, W. Zheng, P. Yuan, L. Qian, and D. Fan: (2004), 6.
[29] J. Zhang, L. Wang, Y. Wu, G. Wang, P. Fu, and Y. Wu: Opt. Express, 19, (2011), 16722.
[30] J.-M. Drezet, S. Pellerin, C. Bezençon, and S. Mokadem: J. Phys. IV, 120, (2004), 299.
[31] L. E. Scriven and C. V. Sternling: Nature, 187, (1960), 186.
[32] E. Allahyari, J. JJ Nivas, E. Skoulas, R. Bruzzese, G. D. Tsibidis, E. Stratakis, and S. Amoruso: Appl. Surf. Sci., 528, (2020), 146607.
[33] V. Lang, B. Voisiat, T. Kunze, and A. F. Lasagni: Adv. Eng. Mater., 21, (2019), 1900151.
[34] S. Xiao, E. L. Gurevich, and A. Ostendorf: Appl. Phys. A, 107, (2012), 333.
[35] A. Cunha, A. P. Serro, V. Oliveira, A. Almeida, R. Vilar, and M.-C. Durrieu: Appl. Surf. Sci., 265, (2013), 688.
[36] J. Bonse, S. Hohm, S. V. Kirner, A. Rosenfeld, and J. Kruger: IEEE J. Sel. Top. Quantum Electron., 23, (2017).
[37] S. Alamri, F. Fraggelakis, T. Kunze, B. Krupop, G. Mincuzzi, R. Kling, and A. F. Lasagni: Materials, 12, (2019), 1018.
[38] A. Sikora, M. Faucon, L. Gemini, R. Kling, and G. Mincuzzi: Appl. Surf. Sci., 591, (2022), 153230.
[39] S. Hou, Y. Huo, P. Xiong, Y. Zhang, S. Zhang, T. Jia, Z. Sun, J. Qiu, and Z. Xu: J. Phys. Appl. Phys., 44, (2011), 505401.
[40] M. Huang, Y. Cheng, F. Zhao, and Z. Xu: Ann. Phys., 525, (2013), 74.
[41] J. Bonse, S. Höhm, A. Rosenfeld, and J. Krüger: Appl. Phys. A, 110, (2013), 547.

(Received: June 3, 2022, Accepted: December 3, 2022)